

# Deep Understanding of the Influence of the Process Parameters During Linear Friction Welding on the Joint Quality and the Microstructural Changes of Two Mono-Material Titanium Alloy Joints: The $\beta$ -Metastable Ti-5Al-2Sn-2Zr-4Mo-4Cr (Ti17) and the Near- $\alpha$ Ti-6Al-2Sn-4Zr-2Mo (Ti6242)



DORICK BALLAT-DURAND, SALIMA BOUVIER, and MARION RISBET

Linear friction welding (LFW) of near- $\alpha$  Ti-6Al-2Sn-4Zr-2Mo (Ti6242) and  $\beta$ -metastable Ti-5Al-2Sn-2Zr-4Mo-4Cr (Ti17) was studied through eight sets of process parameters. Varying the main LFW process parameters revealed that: (1) increasing the ratio between the normal pressure and local flow stress shortens the duration of friction phase (III); this ratio is influenced by the normal pressure and/or heat generated by the longitudinal deformation conditions, the latter being driven by the oscillation parameters (amplitude and frequency); (2) the joint and PAZ extents can be drastically lowered by favoring the extrusion of the heated material through higher normal pressures; (3) the presence of defects is mostly due to contaminant layers initially present on the contact surfaces; these defects can be dissipated into the bulk with the help of an enhanced recrystallization and/or material blending; (4) the two-component  $\{110\}\langle 111 \rangle$   $\beta$  texture intensity is mostly influenced by the amplitude and degree of recrystallization. Subjecting three significantly different Ti17 joints to  $\beta$ -annealing resulted in similar homogenized microstructures and defect dissolution. The different material responses of Ti17 and Ti6242 to LFW showed the necessity of defining optimized sets of process parameters depending on the welded materials and initial microstructures.

<https://doi.org/10.1007/s11661-019-05503-7>

© The Minerals, Metals & Materials Society and ASM International 2019

## I. INTRODUCTION

Ti alloys are now largely used for structural applications in the aeronautic industry because of their advantageous performance-to-density ratio combined with fairly good thermal expansion and electro-chemical compatibility with carbon-fiber reinforced plastics (CFRPs). However, welding Ti alloys using common fusion techniques can be challenging since detrimental atmospheric pollution might occur if sufficient gas shielding is not used; solidification defects and/or pores can also be present. Indeed, oxygen can cause a change from good ductility at low oxygen concentration (0.07 wt pct) to total brittleness at 0.65 wt pct<sup>[1]</sup>; pores due to

hydrogen and CO<sub>2</sub> pollution were also identified within Ti joints obtained by electron beam welding.<sup>[2]</sup> Solid-state joining processes such as linear friction welding (LFW) are believed to prevent the Ti alloy assemblies from being subjected to these issues. Indeed, the literature review of friction welding suggested that Ti alloy LFW joints remained below the liquidus in the  $\beta$  domain, plus only for a very short time, thus avoiding the formation of typical fusion welding defects (*i.e.*, excessive interstitial enrichment or retained pores).<sup>[3]</sup>

In LFW, the heat induced by friction at the rubbing surfaces ultimately results in joining under an appropriate set of axial pressure and oscillating motion contingent upon the geometries and materials constituting the welded parts. LFW configurations are defined by a specific power input parameter and four characteristic process phases<sup>[4]</sup>:

- *Contact stage I*: The two parts are brought into contact initially resting on surface asperities followed by an increase in the contact area due to asperity flattening.

---

DORICK BALLAT-DURAND, SALIMA BOUVIER, and MARION RISBET are with the Sorbonne Universités, Université de Technologie de Compiègne, Laboratoire Roberval de Mécanique, UMR-CNRS 7337, CS 60319 Rue Roger Couffolenc, 60203 Compiègne Cedex, France. Contact e-mail: dorick.ballat-urand@utc.fr

Manuscript submitted May 13, 2019.

Article published online November 4, 2019

- *Initial stage II*: Large particles are expelled from the interface, and the friction on the asperities leads to a local heating forming hot spots initiating material joining and axial shortening.
- *Friction stage III*: The heat and joining extend up to the entire contact interface leading to severe local shear stresses and consistent deformation heating; the joint is no longer able to handle the axial load leading to the material extrusion and consistent axial shortening.
- *Forging stage IV*: Once the axial shortening threshold is reached, the oscillation stops and the weld is consolidated by holding the axial pressure; fast cooling is ensured by heat diffusion within each welded part.

Previous work performed by the authors of this article already characterized the microstructures of mono-material LFW joints using Ti17 and Ti6242.<sup>[5,6]</sup> These studies showed that remarkable gradients of thermo-mechanical loads were present within the weld-enhancing phase transformations and recrystallization/recovery. These phenomena led to the formation of two main characteristic macro-zones: the joint core, which underwent severe thermo-mechanical processing resulting in deep microstructural changes, and the process-affected zone (PAZ), mostly composed of the joint core in the center and two adjacent transitional zones exhibiting microstructures comparable to that of the base material (BM) at meso-scale but displaying affected hardness properties. The literature review indicates that the preliminary studies concerning LFW focused on understanding and modeling the performances and quality of  $\alpha + \beta$  Ti alloy joints.<sup>[7,8]</sup> These investigations were focused on succinct microstructural characterizations and on the identification of a specific power input (PI) as an indicator of the weld soundness. Detailed investigations focusing on the effects of the LFW process parameters on the widely used Ti64 revealed that: (1) both a minimum power input parameter and axial shortening were required to achieve a defect-free sound weld; (2) the retained defects were in the form of oxides and/or pores; (3) an increase in the power input resulted in a significant welding time reduction; (4) the size of the PAZ is mainly driven by the welding time, and a major contribution of an increase in the normal pressure to the PAZ thinning was also noted.<sup>[9]</sup> Such an increase in the normal pressure was also found to result in a significant decrease in the texture of the  $\alpha$  phase in the weld center line.<sup>[10]</sup> To the authors' knowledge, and despite the growing industrial interest in these two commercial Ti alloy grades, such thorough investigations have not been reported so far for LFW, the  $\beta$ -metastable Ti17 forging alloy or the near- $\alpha$  Ti6242 elevated-temperature alloy. In fact, their specific behavior and microstructural changes upon thermo-mechanical processing related to their different alloying compositions and starting commercial microstructures constitute a remarkable opportunity for generalizing the optimization of microstructures resulting from LFW Ti alloys as proposed in the present article.

The main process parameters controlling LFW were varied one parameter at a time from a reference configuration empirically determined from Ti64 samples through the normal pressure, oscillating motion (*i.e.*, the amplitude and frequency) and axial shortening (burn-off). A variation in normal pressure of 30 MPa was chosen in this study according to the differences in flow stresses in the  $\beta$ -domain between the heavily alloyed Ti17 and the less hardened Ti6242 compared with Ti64.<sup>[11]</sup> A variation of  $\pm 1$  mm in amplitude and  $-1$  mm in axial shortening was set because of the relatively large size of the prior  $\beta$  grains in Ti17 and the coarse macro-zones in Ti6242. A variation of  $\pm 10$  Hz in frequency was used to provide intermediate oscillation speed values between the reference configuration and the ones with varied amplitudes. The microstructures, power inputs and friction-phase durations of seven different LFW configurations were studied. The investigations were focused on the evolution of the extent of the weld macro-zones, presence/type of defects and recrystallization/texture development in the  $\beta$  domain. *In fine*, these findings will provide valuable quantitative insights into the literature on LFW for enhancing the removal/disruption of welding flaws, controlling the texture development as well as limiting the extent of the process-affected zone.

## II. MATERIAL AND METHODS

An MDS-30 LFW machine developed by the ACB Company in Nantes, France, was used to produce the joints. Only one process parameter was varied at each welding attempt while keeping the reference values for the other parameters as follows: a frequency ( $F$ ) of 50 Hz, amplitude ( $A$ ) of 2 mm, normal pressure ( $P$ ) of 90 MPa and axial shortening threshold ( $U$ ) of 3 mm. Blocks of  $15 \times 80 \times 70$  mm<sup>3</sup> were used for LFW obtained by electrical discharge machining (EDM) from forged billets ( $R = 250$  mm;  $L = 570$  mm) of TIMETAL<sup>®</sup> 6-2-4-2 and TIMETAL<sup>®</sup> 17, the 80-mm edge being parallel to the billet axis. The specimens were welded on the raw  $15 \times 80$  mm<sup>2</sup> surface, the 80-mm edge being aligned with the oscillation direction. The LFW process parameters of the reference and the seven varied configurations are detailed in Table I; the notations  $X + 1$  indicate an increase in the value of the investigated process parameter and the inverse.

The dimensions of the samples and process axis are detailed in Figure 1. The surface preparation used in this article relied on coarse grid paper polishing, polyester cloth semi-finishing and vibratory finishing.<sup>[5]</sup> The macroscopic investigations were performed using optical microscopy (OM) on an Olympus BX41M and micro-hardness tests on a Zwick-Roell ZHU $\mu$ -S. The microscopic analyses were performed on a Zeiss Sigma scanning electron microscope (SEM) coupled with both electron backscatter diffraction (EBSD) and energy-dispersive X-ray (EDX) spectroscopy systems. The Matlab<sup>®</sup> Mtex 5.1.1 toolbox was used for post-processing the EBSD data. A NABERTHERM P330 oven with an

**Table I. LFW Process Parameters of the Eight Configurations Investigated (Ref + 7);  $P$  Is the Normal Pressure,  $A$  and  $F$  Are the Amplitude and Frequency of the Oscillating Motion, Respectively, and  $U$  Is the Axial Shortening Threshold for Axial Motion Stop**

| Config. | $P$ (MPa)  | $A$ (mm) | $F$ (Hz)  | $U$ (mm) |
|---------|------------|----------|-----------|----------|
| Ref     | 90         | 2        | 50        | 3        |
| $U - 1$ | 90         | 2        | 50        | <b>2</b> |
| $P - 1$ | <b>60</b>  | 2        | 50        | 3        |
| $P + 1$ | <b>120</b> | 2        | 50        | 3        |
| $A - 1$ | 90         | <b>1</b> | 50        | 3        |
| $A + 1$ | 90         | <b>3</b> | 50        | 3        |
| $F - 1$ | 90         | 2        | <b>40</b> | 3        |
| $F + 1$ | 90         | 2        | <b>60</b> | 3        |

Bold values indicate the variation in the process parameter used compared to the reference set.

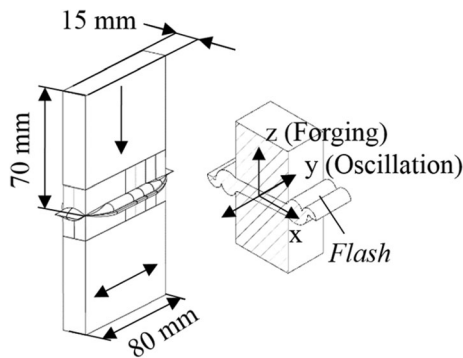


Fig. 1—Sketch of the geometry of the welding process and sampling method for the observations and diffraction analysis<sup>[5]</sup>; the forging part is the upper part ( $z > 0$ ) and the oscillating part is the lower part ( $z < 0$ ).

argon protective atmosphere was used for the post-weld  $\beta$  annealing.

### III. EXPERIMENTAL RESULTS

#### A. Ti17 Reference LFW Joint

The high-strength  $\beta$ -metastable forging alloy Ti-5Al-2Sn-2Zr-4Cr-4Mo (Ti17) used in this study is characterized by a Widmanstätten  $\alpha + \beta$  microstructure with fine entangled  $\alpha$  laths precipitated within large prior  $\beta$  grains (500  $\mu\text{m}$  in diameter). Previous investigations showed that a sound joint was achieved using the reference process parameters detailed in Table I.<sup>[5]</sup>

The  $\beta$  thermo-mechanical processing loads that occurred close to the contact interface resulted in retaining soft  $\beta_{\text{metastable}}$  microstructures in the joint upon cooling. This joint is demarcated by three distinguishable zones: the refined welding line (WL) composed of fragmented  $\beta$  subgrains, the thermo-mechanically affected zone (TMAZ) consisting of severely plasticized large prior  $\beta$  grains and the heat-affected zone (HAZ) exhibiting a partial and

gradual dissolution of the  $\alpha$  precipitates inducing a decrease in hardness from the BM. The  $\beta$  thermomechanical processing and subsequent extreme shear in the WL enhanced the continuous dynamic recrystallization (CDRX) mechanisms to accommodate the plastic deformation. This resulted in the fragmentation of the large prior  $\beta$  grains initially present in the BM into subgrains that ultimately formed recrystallized nuclei. These refined grains exhibit a strong texture with the  $\langle 110 \rangle$  direction almost aligned with the transversal direction  $\langle x \rangle$  and the  $\langle 111 \rangle$  direction parallel to the oscillation direction  $\langle y \rangle$ . An overall microstructure depiction of the Ti17 LFW joint is shown in Figure 2.

#### B. Ti6242 Reference LFW Joint

The elevated temperatures near  $\alpha$  alloy Ti-6Al-2Sn-4Zr-2Mo (Ti6242) in the fully equiaxed state used in this study were characterized by predominant nodular  $\alpha$  grains embedded within a  $\beta$  matrix. The microstructural investigations on a reference joint showed that the thermomechanical processing loads occurring close to the initial rubbing surfaces led to the formation of a hard joint delimited by three specific zones: the WL made of highly textured ultra-fine martensitic  $\alpha'$  laths precipitated within prior  $\beta$  subgrains, the TMAZ consisting of  $\alpha_{\text{secondary}}$  fragments formed within highly deformed former  $\alpha$  nodules with scattered retained  $\beta$  phase and the HAZ, which did not display remarkable microstructural changes from the BM but showed a slightly affected hardness.<sup>[6]</sup> The reconstruction of the  $\beta$  orientations prior to the  $\beta \rightarrow \alpha'$  transformation upon cooling permitted identifying the development of a deformation texture of the  $\beta$  phase during the process similar to the one formed in the WL of Ti17 detailed previously. The martensitic  $\beta \rightarrow \alpha'$  transformation in the WL/near-TMAZ (NTMAZ) upon cooling resulted in a strong  $\{0001\}\langle 11\bar{2}0 \rangle$  texture. This texture is characterized by: (1) the  $\langle 0001 \rangle$  direction being aligned with the transversal direction  $\langle x \rangle$ ; (2) the  $\langle 11\bar{2}0 \rangle$  direction being parallel to the oscillation direction  $\langle y \rangle$ . An overall microstructural depiction of the Ti6242 LFW joint is shown in Figure 3.

#### C. Process Output Analysis

The LFW machine used in this study (MDS30) allowed monitoring the  $\langle y \rangle$  position of the oscillating table and the  $\langle z \rangle$  displacement of the forging part during the process. The analysis of these two data sets enabled the formal identification of the LFW process phases in terms of both durations and extrusion rates with respect to the process parameters. The evolution of the oscillating and forging motions during the process are shown in Figure 4 for both the Ti17 and Ti6242 welds. One can observe three distinct stages occurring during the process for the two materials. The first stage (I) is characterized by a rigid friction; the second stage (II) began by the initiation of the axial shortening starting with a fairly low rate ( $\alpha_{\text{II}}$ ) followed by the third stage (III) displaying a sharp increase in burn-off rate until

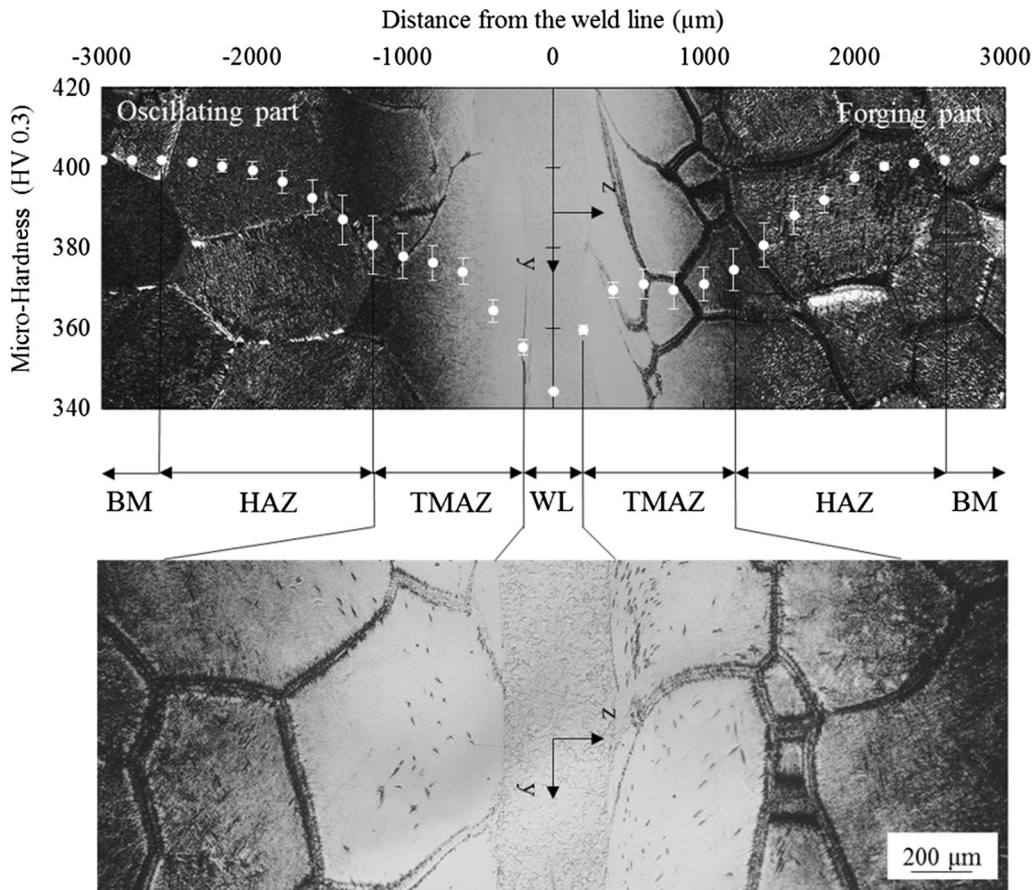


Fig. 2—Bright-field micrographs and associated local hardness values of an etched Ti17 LFW sample (top) showing the three distinct macro-zones: the welding line (WL), thermomechanically affected zone (TMAZ) and heat-affected zone (HAZ); a zoom of the joint core is also provided (bottom) revealing a remarkable microstructure refinement in the WL neighbored by deeply plasticized prior  $\beta$  grains exhibiting an apparent dissolution of their formerly hardening  $\alpha$  precipitates.<sup>[5]</sup>

reaching an apparent steady state ( $\alpha_{III}$ ). These stages actually correspond to the description of the characteristic LFW process phases detailed in the introduction.<sup>[4]</sup>

Several data can be extracted from the graphs in Figure 4 to compare the behaviors of the two Ti alloys as well as to identify the influence of the process parameters on the LFW stages. In this study, the authors intended to investigate the welding process through the durations of the first three process stages (I contact, II initial and III friction) and the two burn-off rates (extrusion initiation  $\alpha_{II}$  and steady-state  $\alpha_{III}$ ). Seven welds using the reference process parameters were obtained; the results are listed in Table II.

The figures in Table II show that both Ti alloys actually displayed similar phase durations for stages I and II while showing slightly different extrusion behaviors during friction stage III. Indeed, the data in Table II indicate that, in the reference configuration, Ti6242 reached the burn-off threshold 1.24 times faster than Ti17 at stage III because of the higher burn-off rates that were about 1.2 ( $\alpha_{II}$ ) and 1.24 ( $\alpha_{III}$ ) times higher in the Ti6242 compared with the Ti17. Similar investigations shown in Figure 5 were conducted on the eight welding configurations (Ref+7) studied in this article (one weld for each varied configuration). The results of

each configuration are also combined with a corresponding specific power input (PI) estimated from the process parameters and defined as follows:  $PI = P \times \dot{\epsilon}$  with  $\dot{\epsilon} = \frac{4 \times A \times F}{L}$  where P is the normal pressure in [MPa],  $\dot{\epsilon}$  is the normalized oscillation speed in [ $s^{-1}$ ] with A being the amplitude in [mm], F the frequency in [Hz] and L the length of the oscillating edge in [mm]. The PI is dimensionally homogeneous to [ $MPa \cdot s^{-1}$ ].

Several major trends can be drawn for both materials from the results shown in Figure 5: (1) the specific power input (PI) appeared to be inversely correlated to the total friction time ( $t_{Friction}$ ); (2) the normal pressure had a major impact on the initial (II) phase and to a lesser extent on the friction (III) phase; (3) the oscillating speed ( $\dot{\epsilon}$ ), apart from being related to the PI, played a remarkable role in the duration of the contact (I) phase by shortening the latter when being increased. Furthermore, the analysis of the variations in the burn-off rates (*i.e.*,  $\alpha_{II}$  and  $\alpha_{III}$ ) revealed the following features: (1) a pronounced proportionality relationship exists between  $\alpha_{II}$  and  $\alpha_{III}$ ; (2) a decrease in PI eventually led to reduced burn-off rates for most of the process configurations. Moreover, the material extrusion sensitivity of the Ti6242 to the PI actually appeared significantly higher than that of the Ti17.

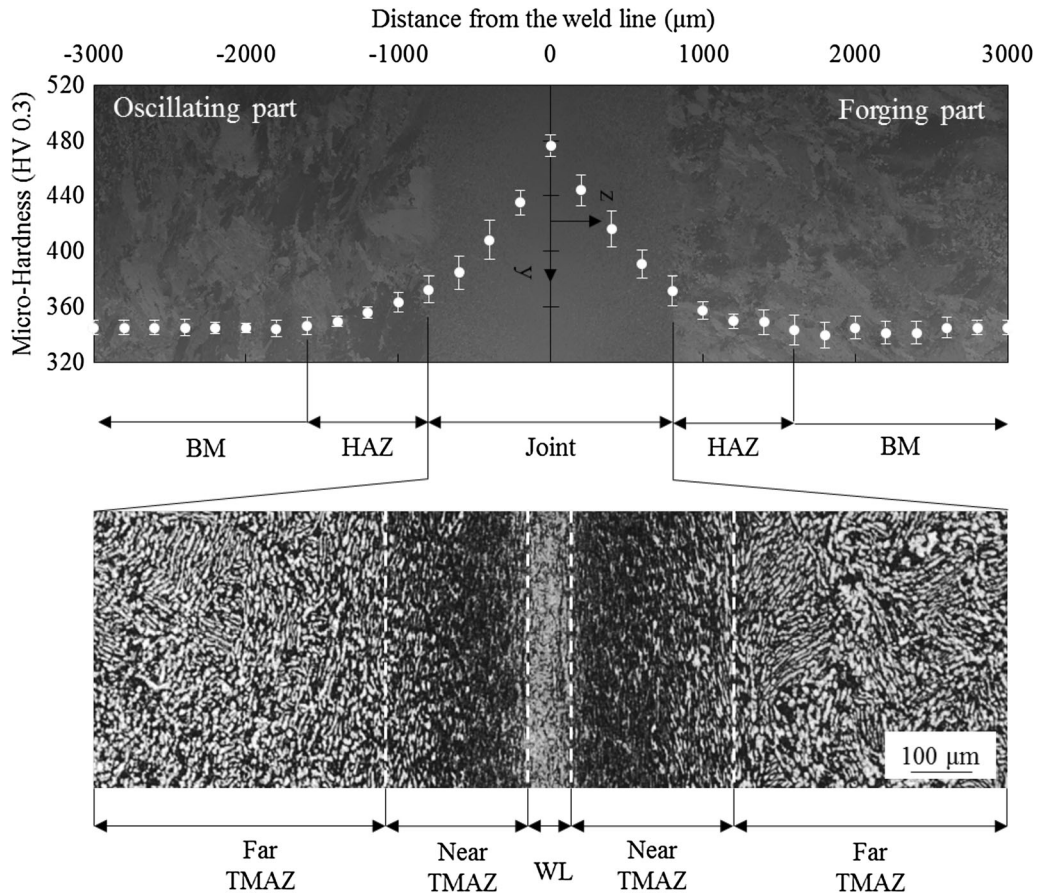


Fig. 3—Polarized-light micrograph (top) and associated local hardness values of an unetched Ti6242 LFW sample showing the presence of a sharp microstructural refinement and consistent joint hardening; a zoom on the etched joint core using bright-field OM (bottom) revealed a further demarcation of the latter into a deeply transformed WL, severely plasticized near-TMAZ (NTMAZ) and just deformed far-TMAZ (FTMAZ).<sup>[6]</sup>

It has been shown here that changes in the process parameters led to remarkable variations in the specific power input, which resulted in shortened LFW process phases when the PI was increased. This shortening is a direct consequence of an increase in burn-off rates due to changes in local thermo-mechanical conditions affecting the material behavior. As a result, the as-welded (AW) microstructures and joint quality were also expected to be deeply affected by these thermo-mechanical processing variations and had to be subjected to extensive inspection endeavors: macro-zones width estimation, defect characterization as well as quantification of the degree of recrystallization and texture development.

#### D. Macro-Zones and Defect Analysis

The results from the meso-scale investigations are summarized in Figure 6. The PAZ extent was determined to be the distance where the local hardness reached a plateau equivalent to the hardness of the BM ( $\pm 2$  pct). The width of the severely transformed macro-zone, namely the joint, was set on Ti17 as the distance between the clear distinction of the regain of the  $\alpha$  laths on either side of the weld center line (as shown in Figure 2). In Ti6242, the central band

exhibiting brisk microstructural refinement was used to set the joint width (as shown in Figure 3). The presence of defects was also identified as specific fine black particles and/or voids scattered along the weld centerline distinguishable from the surrounding “clean” microstructure.

The widths of both the joint core and PAZ exhibited fluctuations similar to those seen on the friction phase (III) durations in Figure 6. The following general trends could be noted for both alloys: (1) the longer the friction phase the wider the macro-zones; (2) a shortened friction phase in the aborted configuration ( $U - 1$ ) led to a thinner weld; (3) changes in the normal pressure resulted in the highest thickness fluctuation for both alloys between  $P - 1$  and  $P + 1$ ; this effect was even sharper for the PAZ of Ti6242. The specific oscillation speed  $\dot{\epsilon}$  appeared to affect the two alloys differently: an increase in  $\dot{\epsilon}$  resulted in a thinned joint and widened PAZ for Ti6242 and inversely for Ti17. Increasing the amplitude led to friction phase durations equivalent those of the  $P + 1$  configurations (using similar PI) in both alloys. However, this increase in amplitude induced a significant increase in the PAZ widths (Ti17: + 30 pct; Ti6242: + 122 pct) as well as in the joint widths but to lesser extents (Ti17: + 20 pct; Ti6242: + 15 pct).

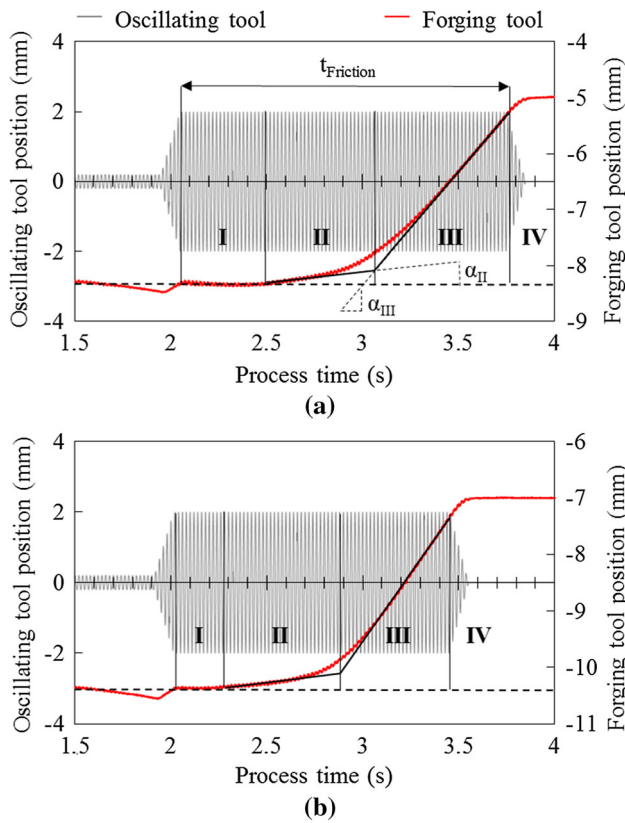


Fig. 4—LFW process outputs for the reference configuration of (a) Ti17 and (b) Ti6242 showing the following stages: rigid friction I; axial shortening initiation II and steady-state III; oscillation stop and weld consolidation IV.

**Table II. LFW Stage Durations and Material Extrusion Rates for the Reference Configuration of (a) Ti17 and (b) Ti6242 Showing the Different Responses to LFW of the Two Ti Alloys Tested**

| (a) Ti17   |       |        |         |                      |                       |
|------------|-------|--------|---------|----------------------|-----------------------|
|            | I (s) | II (s) | III (s) | $\alpha_{II}$ (mm/s) | $\alpha_{III}$ (mm/s) |
| Mean       | 0.45  | 0.56   | 0.67    | 0.59                 | 3.98                  |
| $\sigma$   | 0.07  | 0.09   | 0.01    | 0.11                 | 0.07                  |
| (b) Ti6242 |       |        |         |                      |                       |
|            | I (s) | II (s) | III (s) | $\alpha_{II}$ (mm/s) | $\alpha_{III}$ (mm/s) |
| Mean       | 0.48  | 0.49   | 0.54    | 0.71                 | 4.96                  |
| $\sigma$   | 0.22  | 0.15   | 0.02    | 0.33                 | 0.11                  |

Additional information indicating the presence of defects within the weld center line showed that only Ti17 did not exhibit defects in the reference configuration. Generally, “clean” welds were the ones satisfying a  $PI \geq 500 \text{ MPa}\cdot\text{s}^{-1}$  combined with a critical burn-off threshold  $U \geq 3 \text{ mm}$ . These defects are the most critical features in LFW as they can jeopardize the mechanical strength of the assembly. The origins of these specific objects were investigated by means of micro-scale observations

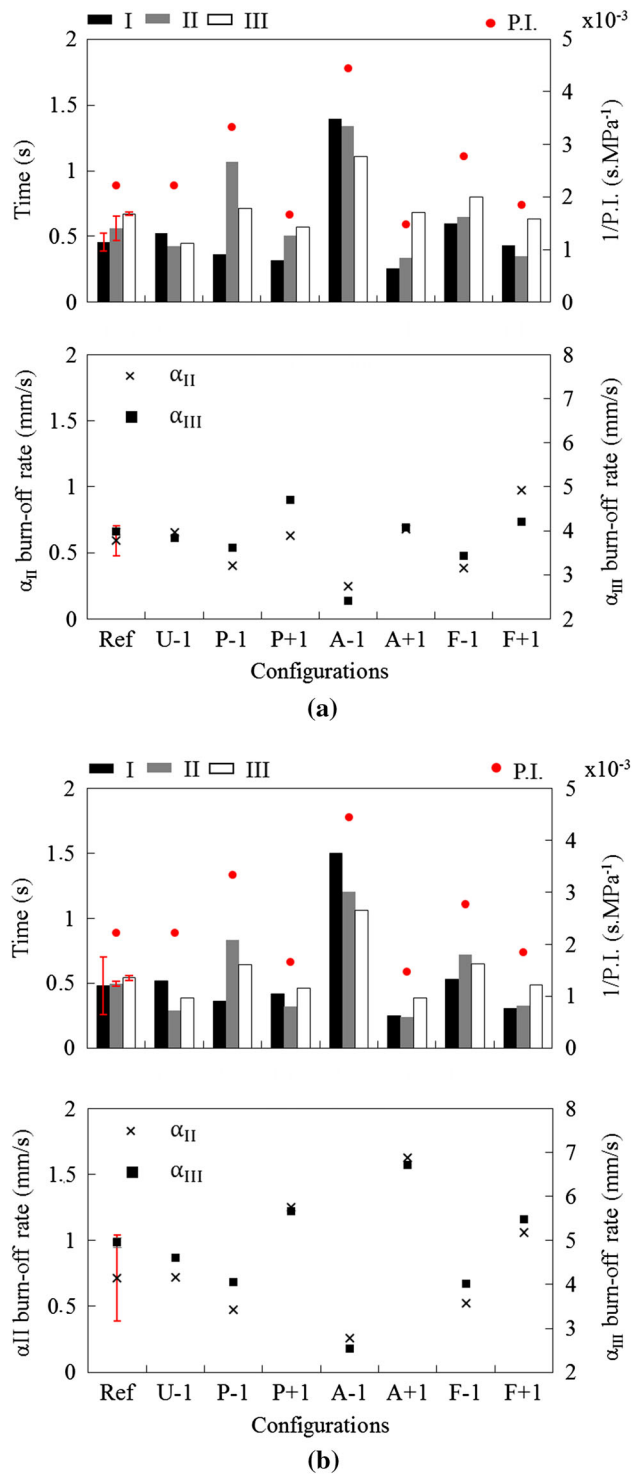


Fig. 5—LFW stage duration and material extrusion rates for the eight configurations tested showing the evolutions in (a) Ti17 and (b) Ti6242 combined with the specific power input used in each case.

combined with diffraction and chemical analysis. Two LFW configurations were compared for both alloys: the one most affected by flaws ( $A - 1$ ) and one free from visible defects ( $A + 1$ ). These two configurations exhibit

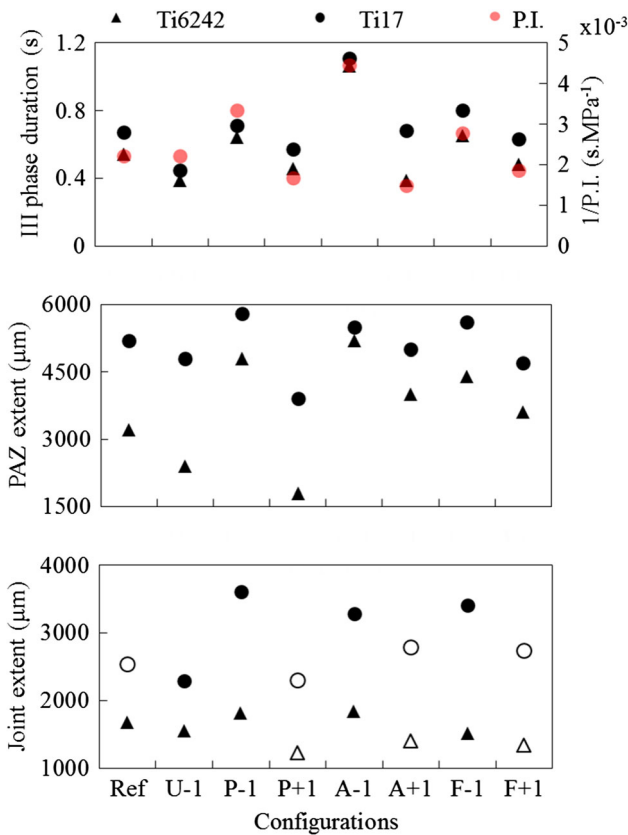


Fig. 6—Estimation of the widths of the joint and PAZ combined with information on the duration of the friction phase and corresponding specific power input (PI) for the eight tested configurations on both Ti17 and Ti6242 alloys. The white markers are used to identify defect-free joints.

the highest differences in terms of PI, oscillation speed and friction time. The SEM micrographs at  $\times 1500$  and the corresponding EDX diffractograms are shown in Figures 7 and 8 for Ti17 and the Ti6242, respectively.

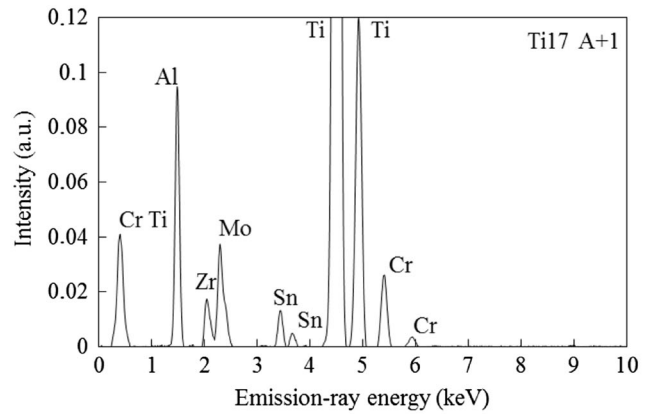
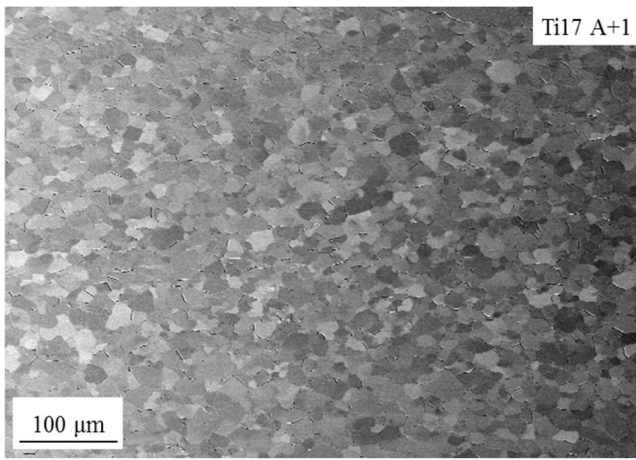
The investigations on the low PI configurations ( $A - 1$ ) showed the presence of fine voids forming along a line corresponding to the weld center line in both alloys. Interspersed isolated clusters of nodular particles were also distinguishable from the surrounding martensitic microstructure in Ti6242. The EDX analysis permitted identifying the presence of copper in the weld with apparent flaws, which is not part of the chemical composition of Ti17 or Ti6242. No voids or special objects were found in the “clean” welds showing only the known alloying elements on the EDX diffractograms. A detailed analysis of one flaw within the  $A - 1$  Ti6242 weld is shown in Figure 9 combining SEM, EBSD and EDX mapping performed on one cluster of nodular particles enclosed within the martensitic microstructure. These investigations evidenced the coexistence of voids (marker 1), nodular hexagonal close-packed (HCP)  $\alpha$  indexed grains (marker 3; gray/green) with interspersed particles of intermetallic  $Ti_2Cu$  (marker 4; red) and body-centered cubic (BCC)  $\beta$  indexed matrix (marker 2; bright/blue) within the martensitic microstructure of the WL (marker 5). Furthermore, a qualitative analysis over the cluster

comparing the local intensity with the global signal of the EDX mapping highlighted a loss of Al and Mo within the nodules and a significant enrichment of Cu/Mo located in the bright matrix plus a slight loss of Ti. These abnormal microstructures appeared quite similar to solidification-like morphologies.

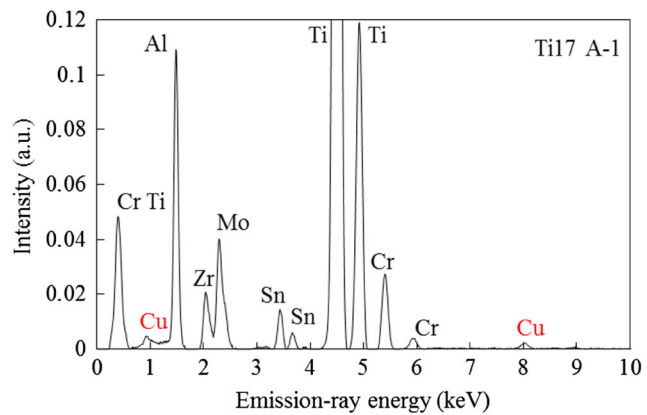
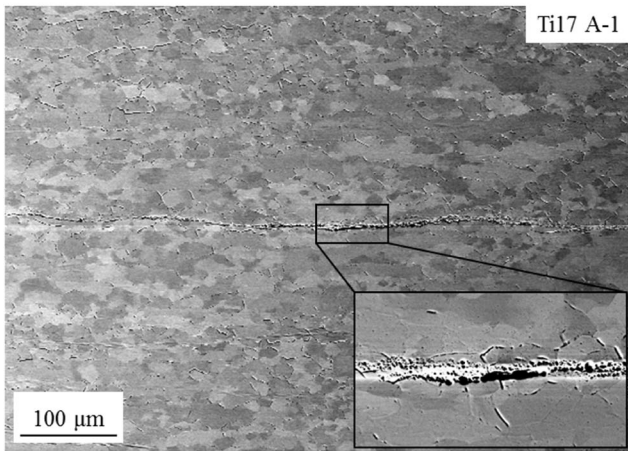
#### E. Material Flow, Texture and Recrystallization

The changes on the thermomechanical conditions induced by varying the welding configurations had major consequences at the meso-scale on both the extents of the characteristic LFW joint zones and the presence of defects. Thus, these changes were also expected to deeply affect the recrystallization mechanisms and the texture developments justifying a detailed investigation of these two quantities. However, the analysis of the welds required a specific analysis as Ti17 retained the  $\beta$  microstructure formed during LFW at room temperature, while Ti6242 experienced a martensitic  $\beta \rightarrow \alpha'$  transformation upon cooling. The preceding investigation revealed that both Ti17 and Ti6242 exhibited similar textural developments of the  $\beta$  phase in the joint core during LFW due to comparable local deformation conditions in the  $\beta$ -domain.<sup>[5,6]</sup> The authors proposed a semiquantitative analysis of Ti17 and Ti6242 joints with the help of a  $\beta$ -microstructure reconstruction algorithm developed in previous work.<sup>[6]</sup> This self-developed sub-routine computes and compares the possible variants of  $\beta$  parent orientations from  $\alpha'$  clusters using the Burgers orientation relationship (BOR) to reconstruct the actual parent prior  $\beta$  grain. A representative  $\beta \{110\}\langle 111 \rangle$  texture developing in the WL of the reference Ti17 joint is shown in Figure 10; a similar texture was observed in Ti6242.

The apparent two-component  $\beta$  texture in the WL shown in Figure 10 is actually formed by two intermediate orientations ( $\beta_{WL}$  and  $\beta_{TWIN}$ ) resulting from the overlapping of two main orientations ( $\beta_{FRG}$  and  $\beta_{OSC}$ ) and their respective twin-symmetric components ( $\beta_{TW\_FRG}$  and  $\beta_{TW\_OSC}$ ). This effect is due to a blending in the WL of independent texture components formed in each near-TMAZ ensuring: their  $\langle 111 \rangle$  directions aligned with  $\langle y \rangle$  and the  $\langle 110 \rangle$  directions slightly misaligned with  $\langle x \rangle$  and  $\langle z \rangle$  for the forging part and the oscillating part, respectively. Furthermore, the grain fragmentation by continuous dynamic recrystallization (CDRX) might also influence the texture intensity and the appearance of such intermediate texture components ( $\beta_{WL}$  and  $\beta_{TWIN}$ ) due to crystallite rotation from the ideal parent orientations ( $\beta_{FRG}$ ,  $\beta_{OSC}$ ,  $\beta_{TW\_FRG}$  and  $\beta_{TW\_OSC}$ ). A preliminary analysis was performed on the texture evolution in the WL in both alloys for all the process configurations to: (1) characterize the influence of the process parameters on the texture intensity; (2) highlight probable heterogeneities between the two intermediate texture components ( $\beta_{WL}$  and  $\beta_{TWIN}$ ). The spots forming the inner ring within the 110 pole figures highlighted in Figure 10 were subjected to a specific analysis to compare the orientation density of all the LFW configurations (Figure 11).



(a)



(b)

Fig. 7—SEM observations in the weld center line of (a)  $A + 1$  and (b)  $A - 1$  Ti17 configurations with the corresponding local EDX diffractograms showing the presence of defects in  $A - 1$  associated with an abnormal presence of copper in the joint. The peak intensity is normalized by the intensity of the highest one. In the micrographs  $\langle z \rangle$  is pointing north and  $\langle x \rangle$  is pointing west.

The following major trends could be noted from the texture analysis in Figure 11: (1) the texture development is more intense in Ti6242 than in Ti17; (2) an increase in the texture intensity and component heterogeneity can be noted for the aborted configuration ( $U - 1$ ) as well as when decreasing the pressure from  $P + 1$  to  $P - 1$ ; (3) varying the longitudinal deformation resulted in lowering the texture intensity for both  $A + 1$  and  $A - 1$ . A decrease in the amplitude also increased the texture component heterogeneity and reciprocity. Nevertheless, these data could not provide information about a potential blending of the texture component or knowledge about the degree of microstructural fragmentation. As a result, the authors proposed conducting a semiquantitative analysis of the spatial distribution of each reference orientation ( $\beta_{FRG}$ ,  $\beta_{OSC}$ ,  $\beta_{TW\_FRG}$  and  $\beta_{TW\_OSC}$ ) and of the grain refinement for all the LFW configurations tested. The aim was to quantify the microstructural changes by the mean of two main indicators: (1) the grain refinement using the area ratio of subgrains formed by CDRX; (2) the texture blending using the share of the boundaries delimiting

different textural components weighted by the grain refinement. An example is showed in Figure 12 for the two configurations exhibiting the largest differences in terms of PI and friction phase duration:  $A - 1$  and  $A + 1$ .

Remarkable microstructural differences between the  $A - 1$  and  $A + 1$  configurations as well as between both alloys can be observed in Figure 12. Indeed, varying the amplitude had major impacts on the resulting microstructures as this parameter seemed to play a key role in the grain fragmentation as well the texture component blending: a low amplitude hindered the formation of subgrains associated with a poor blending of the texture and the inverse. In addition, fundamental microstructural differences could be noted between both alloys as the grain fragmentation in Ti17 appeared to be highly sensitive to the deformation conditions compared with Ti6242. Figures 12a and b shows that Ti17 forming quasi-uniform texture strata for  $A - 1$  led to poor blending compared with a deeply fragmented and mixed microstructure for  $A + 1$ . However, the microstructure in the Ti6242  $A - 1$  configuration didn't reveal any



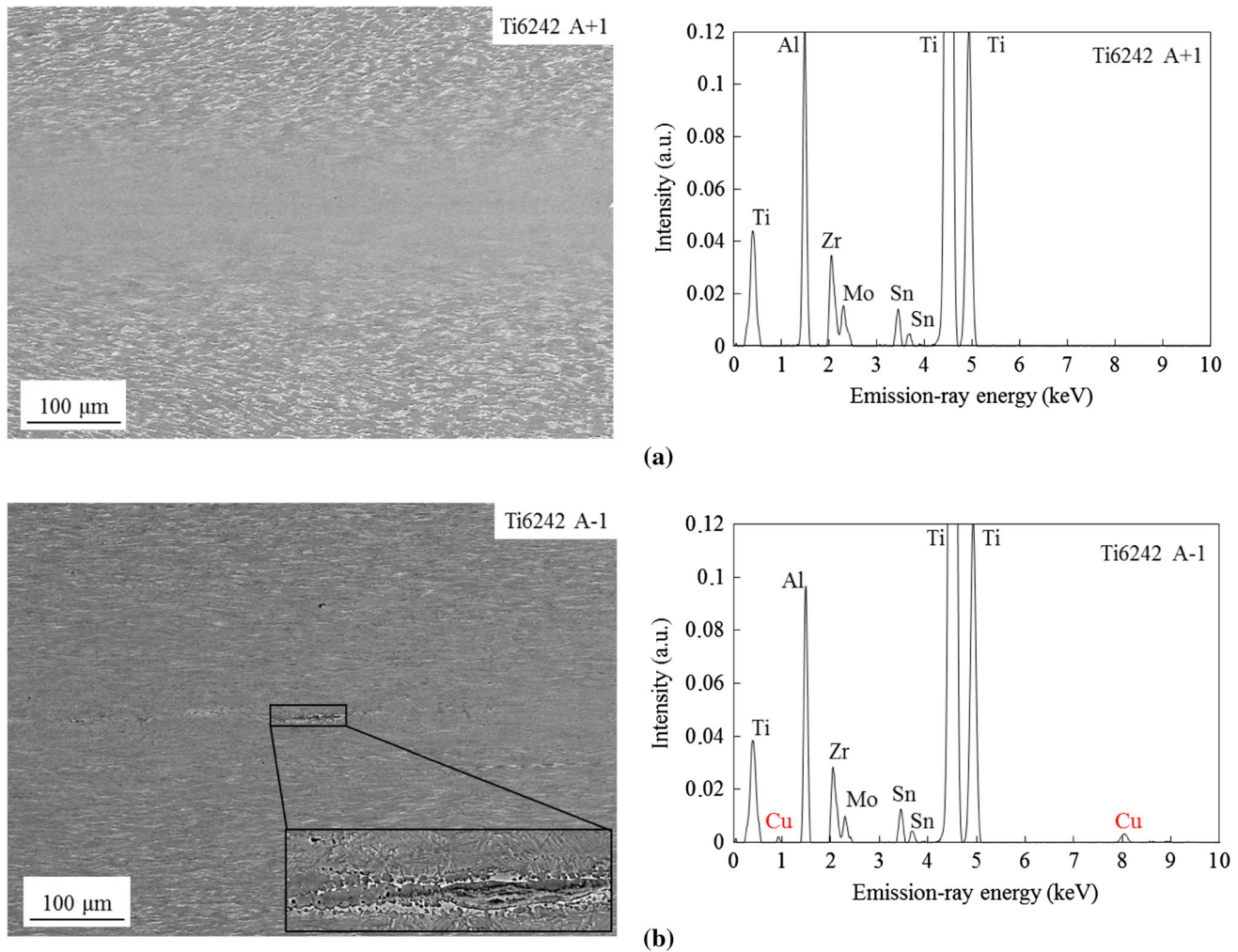


Fig. 8—SEM observations in the weld center line of (a)  $A + 1$  and (b)  $A - 1$  Ti6242 configurations with the corresponding local EDX diffractograms showing the presence of abnormal microstructural objects in  $A - 1$  associated with a parasitic presence of copper in the joint. The peak intensity is normalized by the intensity of the highest one. In the micrographs  $\langle z \rangle$  is pointing north and  $\langle x \rangle$  is pointing west.

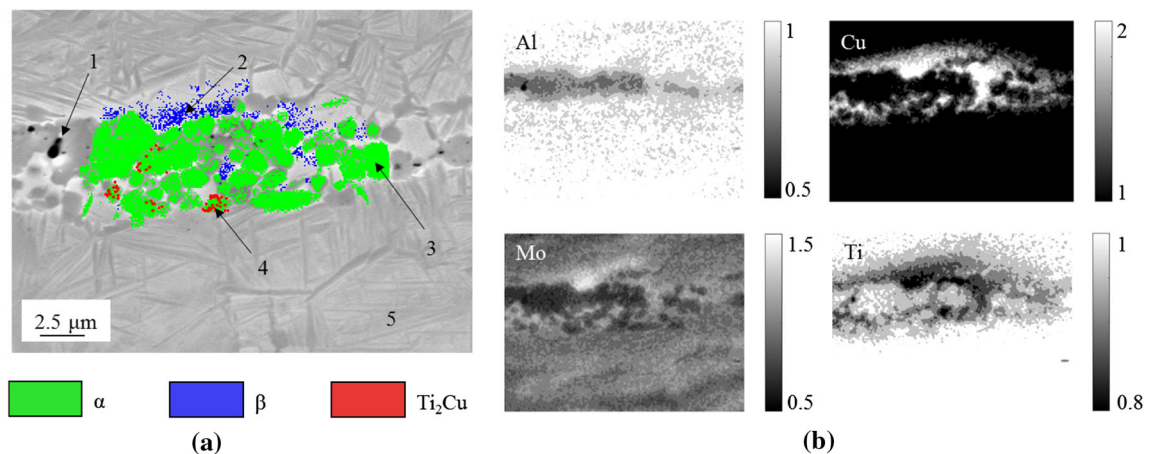


Fig. 9—Multi-technique investigations on the abnormal microstructural formation within the  $A - 1$  Ti6242 joint combining crystallographic/phase identification with chemical analysis showing: (a) a SEM micrograph overlapped with the local EBSD phase identification; (b) the corresponding EDX intensity map of the most affected chemical component distributions, with  $\langle z \rangle$  pointing north and  $\langle x \rangle$  pointing west (Color figure online).

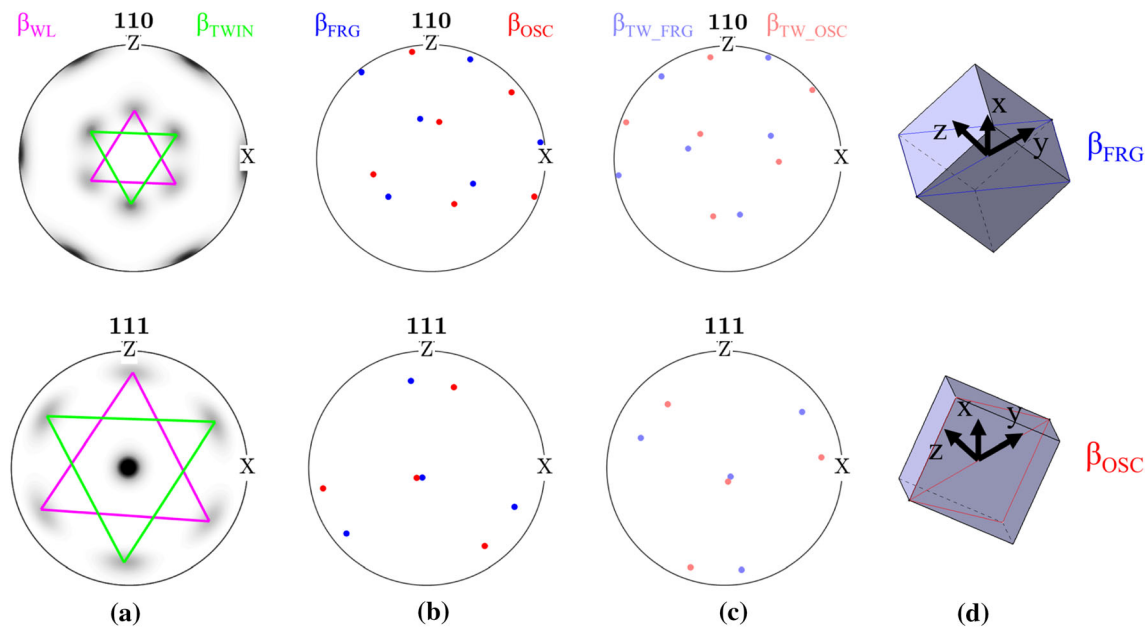


Fig. 10— $\beta$  phase  $\{110\}\langle 111 \rangle$  texture within the WL after welding with (a) the experimental two-component texture from a Ti17 reference weld; (b) the intermediate component ( $\beta_{WL}$ ) composed by two independent textures developing separately in the near-TMAZs of the forging part ( $\beta_{FRG}$ ) and in the oscillating part ( $\beta_{OSC}$ ); (c) the respective twin-symmetric component formation ( $\beta_{TW\_FRG}$  and  $\beta_{TW\_OSC}$ ); (d) the schematic ideal lattice orientations of  $\beta_{FRG}$  and  $\beta_{OSC}$ .

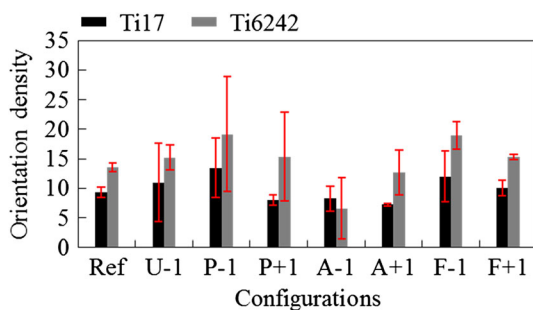


Fig. 11—Evolution of the texture intensity of the  $\beta$  phase from the 110 pole figures and the heterogeneity between the two main symmetric components ( $\beta_{WL}$  and  $\beta_{TWIN}$ ) obtained within the WL of the eight tested configurations on both alloys. Only the maximum density of each spot forming the inner ring in the 110 pole figures was considered (odf half-width = 2 deg). The data were obtained from EBSD scans performed on zones of  $1000 \times 400$  and  $200 \times 400 \mu\text{m}^2$  within the joint core of Ti17 and Ti6242, respectively.

strata of large grains but a rather fine  $\beta$  microstructure, which was also characterized by a relatively poor blending. A significant increase in grain fragmentation and improved spatial distribution of the texture component were also achieved in Ti6242  $A + 1$ . The different initial microstructures and mechanical properties might be responsible for such a discrepancy in the microstructural changes.

The investigations on the microstructural refinement and material blending for all the LFW configurations are displayed in Figure 13. The results revealed that: (1) the microstructural changes in Ti17 were more sensitive to the thermo-mechanical processing conditions than in Ti6242; (2) aborting a test ( $U - 1$ ) or lowering the PI

resulted in a decrease in grain fragmentation and lowered texture blending; (3) an enhanced microstructural refinement by increasing the PI resulted in better mixing with a major impact of the amplitude parameter in both alloys; (4) the changes in frequency ( $\pm 10$  Hz) performed here had only minor impacts on the microstructural features of the WL. Furthermore, combining the texture intensity data from Figure 11 with the recrystallization/blending information detailed above revealed an apparent relationship between the texture component heterogeneity and blending indicator. The texture intensity also appeared to be correlated to the degree of CDRX. Yet a specific behavior can be seen for  $A - 1$  as the texture is lower than the one in the reference while exhibiting poor grain fragmentation.

Previous studies on the Ti17 and Ti6242 joints showed that the metastable microstructures formed upon LFW experienced considerable changes when subjected to the post-weld heat treatment (PWHT) due to grain growth of the recrystallized  $\beta$  nuclei and activation of recovery mechanisms in the TMAZ.<sup>[5,6]</sup> As a result, a succinct analysis was conducted to determine the texture intensity in the former WL after grain growth and to qualify the homogenization capacity of the welds. Three characteristic Ti17 configurations (Ref,  $A - 1$  and  $A + 1$ ) were investigated after a heat treatment in the  $\beta$ -domain ( $910^\circ\text{C}$  for 2 h) followed by water quenching to retain a single-phase  $\beta$  microstructure at room temperature. The resulting grain orientation maps and corresponding 110 and 111 pole figures for the mean grain orientations within the former WLs are displayed in Figure 14.

The EBSD analysis of the heat-treated joints shown in Figure 14 revealed a remarkable grain growth that

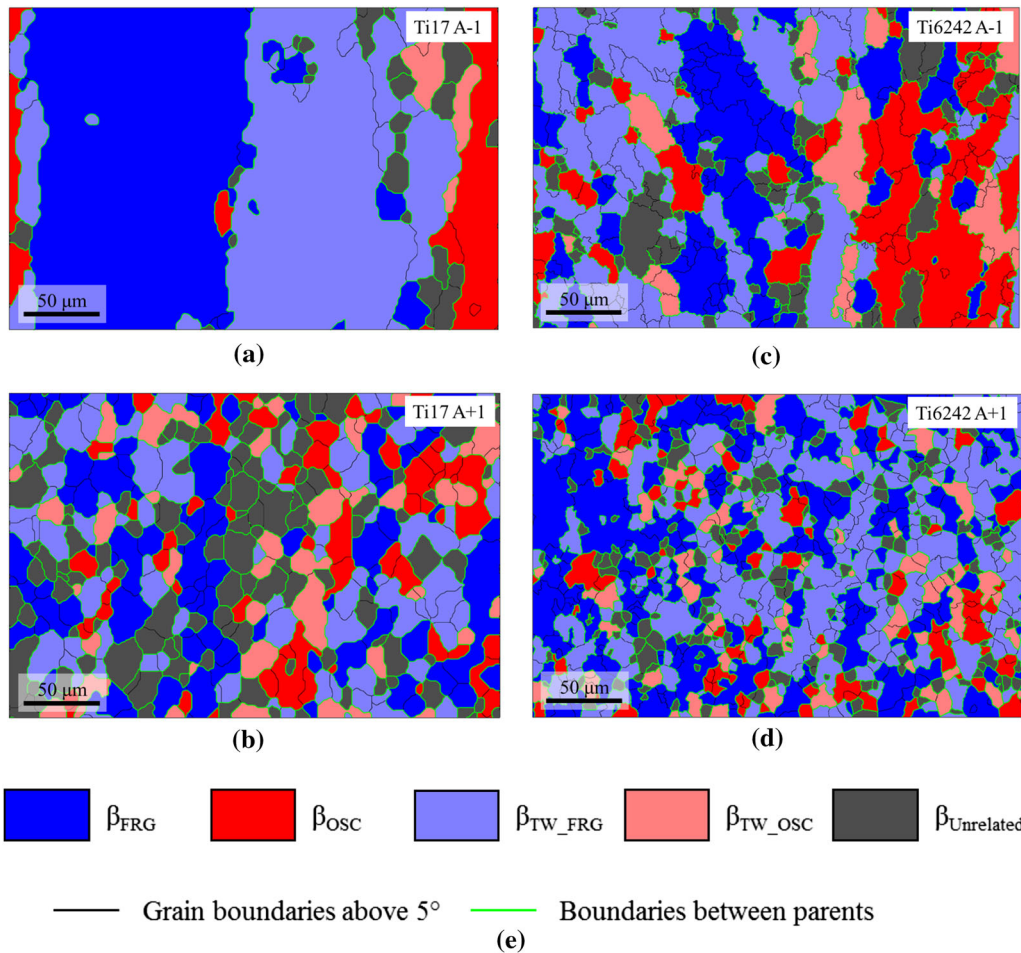


Fig. 12—Spatial distribution of the ideal  $\beta$  texture components (*i.e.*,  $\beta_{FRG}$ ,  $\beta_{OSC}$ ,  $\beta_{TW\_FRG}$  and  $\beta_{TW\_OSC}$ ) within the joint core obtained from EBSD orientation maps for (a) Ti17  $A - 1$ ; (b) Ti17  $A + 1$ ; (c) Ti6242  $A - 1$ ; (d) Ti6242  $A + 1$ ; (e) legend, with  $\langle y \rangle$  pointing north and  $\langle z \rangle$  pointing west.

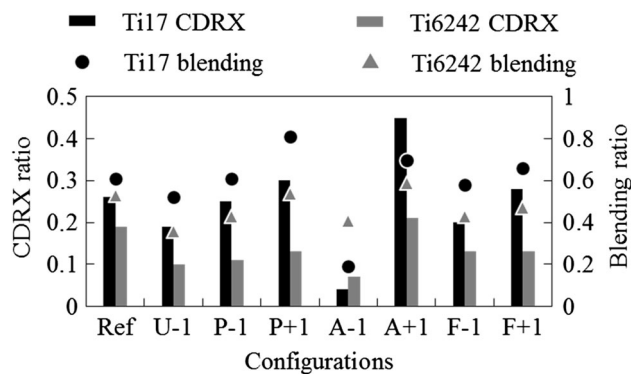


Fig. 13—Semiquantitative analysis characterizing the degree of microstructural refinement by grain fragmentation (CDRX) and texture blending in the WL of Ti17 and Ti6242 for the eight tested LFW configurations. The data were obtained from EBSD scans performed on zones of  $1000 \times 400$  and  $200 \times 400 \mu\text{m}^2$  within the joint core of Ti17 and the Ti6242, respectively.

locally homogenized the microstructure in the form of large equiaxed  $\beta$  grains in place of the former distinct as-welded macro-zones. Similar microstructures were

formed in the three cases studied (Ref,  $A - 1$  and  $A + 1$ ). Moreover, the defects initially present in the  $A - 1$  configuration were no longer visible, and no specific grain boundary pinning could be identified in the heat-treated microstructures.

## IV. DISCUSSION

### A. Process Phases

The dry contact friction in stage I initiating LFW is characterized by highly concentrated heat generation at the surface asperities. However, bonding is hindered in the early process stages because of the surface roughness and intervening contaminant layers preventing proper metal/metal contact.<sup>[12]</sup> Removing the contaminant layers through particle extrusion is believed to establish bonding on the asperities by electron transfer and would lead to extreme shear at these local junctions. Such a localized plastic deformation would result in remarkable heat generation by energy dissipation.<sup>[12]</sup> The combined effects of an increase in temperature with asperity flattening would lead to an escalation in the contact

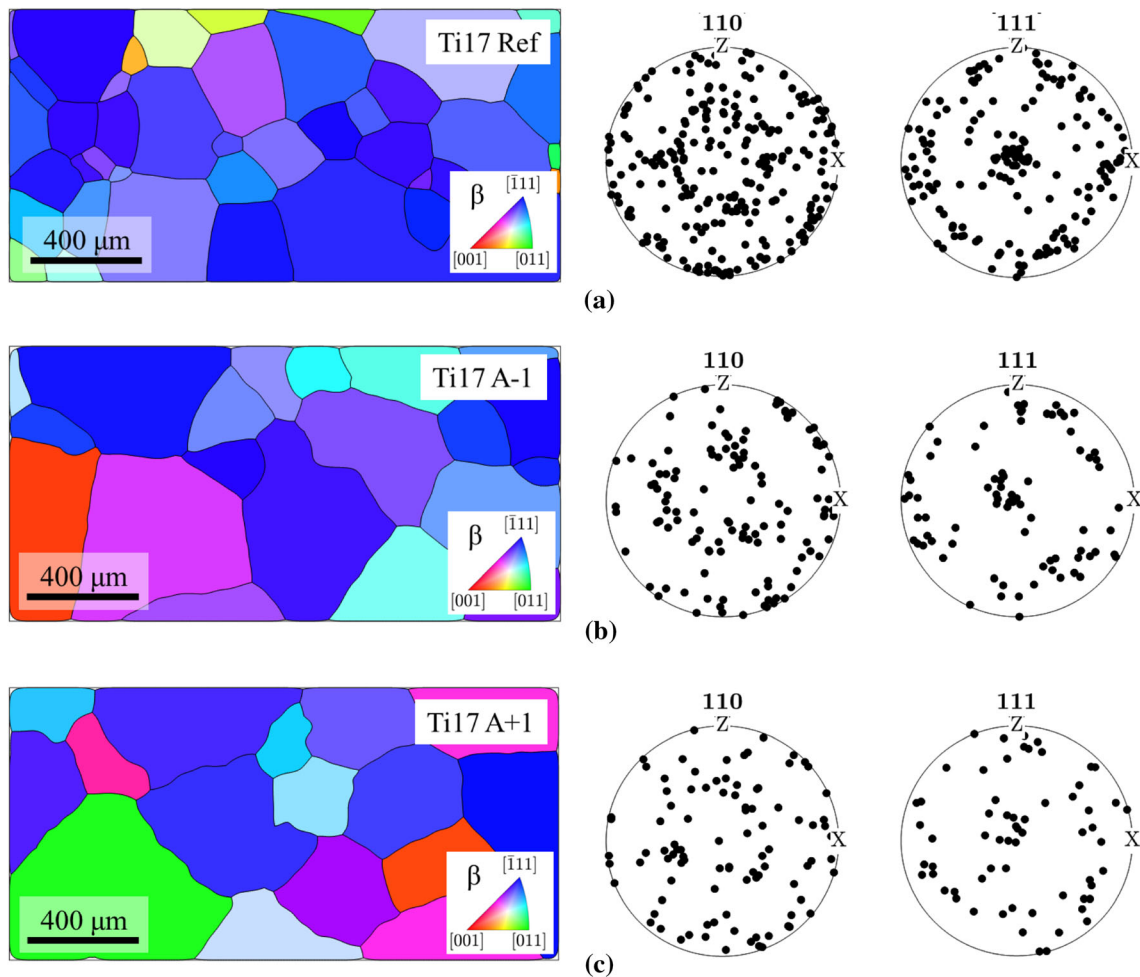


Fig. 14—EBSD mean grain orientation maps of the former joint core after a heat treatment in the  $\beta$ -domain allowing  $\beta$  grain growth and the corresponding orientations in the 110 and 111 pole figures for (a) Ti17 Ref; (b) Ti17 A - 1; (c) Ti17 A + 1. The colors indicate the crystallographic directions of the BCC  $\beta$  phase along the  $\langle y \rangle$  direction;  $\langle x \rangle$  is pointing east and  $\langle z \rangle$  is pointing north (Color figure online).

area and might ultimately result in vacuum contact friction causing rapid global bonding. This phenomenon would switch the heat generation origin from contact friction to internal friction (*i.e.*, plastic deformation). However, a melting wear of the contaminant layers could delay or jeopardize the global joining by preventing the two sliding surfaces from creating metal/metal bonds until this liquid layer is expelled or decomposed into the bulk. The results obtained in this study allowed identifying remarkable changes in the contact stage (I) durations mostly when varying the oscillation conditions through the amplitude or the frequency; no particular features were observable on the effect of the normal pressures tested here. Indeed, the oscillation speed appeared to play a key role in shortening the rigid contact friction stage when being increased and the reciprocal; this might help the contact interfaces to reach higher temperatures thus enhancing the extrusion/decomposition of the contaminants. Yet traces of the latter could still be found in the weld center line for low PI configurations even after a large axial shortening

( $U > 3$  mm); this will be subjected to specific discussions.

Stages II and III appeared quite correlated in terms of both durations and extrusion rates as both are driven by the material extrusion behavior and heat generation/diffusion. Thus, the configurations ensuring an increase in PI resulted in shorter process phases due to higher extrusion rates. The results highlighted the presence of competing mechanisms between the normal pressure, which forces the viscous material out of the joint and the oscillating motion driving the heat generation in the joint. Therefore, several levers can be taken into account to shorten stages II and III through an enhanced extrusion ability. To do so, the ratio between the normal pressure and local flow stress should be increased by either using higher forging pressures and/or ensuring an intensified heat generation; the latter appeared to be mostly driven by the oscillating conditions (amplitude and frequency). Furthermore, the released energy from recrystallization mechanisms might have also played a role in shortening stages II and III by increasing the

temperature in the joint.<sup>[13]</sup> The effect on the resulting microstructures will be the subject of a specific discussion. Moreover, the aborted configuration  $U - 1$  (*i.e.*, reduced burn-off) exhibited a burn-off rate  $\alpha_{III}$  similar to the one of the reference while revealing microstructural features (*i.e.*, textures, recrystallization and blending) quite different from those obtained with the reference. This revealed the absence of a steady state in the microstructural changes between  $U - 1$  and the reference despite showing analogous extrusion rates.

As a result, one can conclude that the mechanisms determining the stage durations between I and II/III are remarkably different and might imply the use of different sets of process parameters optimized for: (1) particle/melting wear removal; (2) shear heating and extrusion. In addition, both Ti alloys tested (Ti17 and Ti6242) revealed similar behaviors to LFW but exhibited rather different sensibility to changes in the process conditions. This could be explained by initial differences in the material features as: (1) the flow stress; (2)  $\beta$ -transus; (3) initial microstructures; (4) passive layer nature; (5) texture development/recrystallization ability. The most detailed investigation conducted in<sup>9</sup> on the widely studied LFW Ti64 joints obtained results consistent with the ones shown in this article, such as stage III can be shortened by increasing the frequency and the amplitude with a process time escalation for amplitudes  $< 2$  mm.

### B. Joint Width

LFW led to significant microstructural changes impacting the extent of the joint macro-zones distinguished by two main regions: the joint core exhibiting remarkable microstructural changes and the PAZ delimiting changes in the local hardness from that of the as-received BM. The investigations conducted in this study revealed that the process parameters played a key role in the extent of these macro-zones depending on the material response to the welding configurations and duration of stage III. Indeed, the competition between heat generation and heat source removal (flash formation) is expected to be the lever for optimizing the joint width as these two forces influence the heat transmitted to the rest of the assembly. However, one should distinguish each process parameter separately as  $P + 1$  and  $A + 1$ , even though they exhibited similar PIs and seemingly correlated analogous process durations, which led to significantly different macro-zone extents in each case, questioning the use of such indicators for comparing the welds.

Increasing the normal pressure resulted in faster extrusion rates leading to a reduction in the process duration due to enhanced material removal. This was caused by a larger extent of heated material experiencing local flow stresses lower than the normal input pressure. Consequently, the heat source is more localized in this case than in the reference combined with a lower friction time, thus reducing the amount of energy transmitted to the rest of the assembly. Such lowered heat generation led to a thinner joint and the inverse. Nevertheless, increasing the normal pressure also implied higher plastic deformation at the weld center influencing recrystallization and consistent heat generation favoring

local material extrusion. On the other hand, varying the oscillating motion through higher longitudinal displacement and/or speed ( $A + 1$  and  $F + 1$ ) led to enhanced extrusion rates and lower process durations than the reference but resulted in a slightly wider joint. This effect could be attributed to the excess of heat produced resulting from the significant increase in shear deformation and the combined effect of recrystallization mechanisms. Inversely, the slow oscillating configurations ( $A - 1$  and  $F - 1$ ) lowered the extrusion ability. The simulations of LFW reported for Ti64 in the literature revealed that this effect could be due to lower temperatures in the weld center (low strain and low recrystallization)<sup>[14]</sup>; lower temperatures imply longer process times and consistent heat diffusion in both parts leading to widened macro-zones.

The differences in joint width between both alloys could be explained by the disparity in terms of  $\beta$ -transus, 890 °C and 990 °C for Ti17 and Ti6242, respectively. Indeed, the heat flux measured for both LFW reference joints, Ti17 and Ti6242, appeared rather similar but the higher  $\beta$ -transus in Ti6242 resulted in thinner macro-zones compared with Ti17.<sup>[5,6]</sup> However, the material responses to LFW were quite dissimilar as the sensitivity to the process conditions of Ti6242 appeared more pronounced than that of Ti17. This might be due to the higher flow stresses of Ti17 compared with those of Ti6242 in the range of thermomechanical processing loads involved during LFW. The contrasting microstructures developing in the TMAZs of each alloy can also influence this behavior as: the  $\beta$  grains forming in the TMAZ of the Ti6242 are 20 times smaller than the prior  $\beta$  grains in Ti17. Indeed, large grains were shown to be less prone to grain reorientation, which hinders the proper alignment of the slip systems with the deformation conditions.<sup>[13]</sup> This behavior would impede the texture development and resulting material flow, thus influencing the burn-off rates ( $\alpha_{II}$  and  $\alpha_{III}$ ). Lower extrusion capability would lead to longer process times, higher heat diffusion and larger macro-zones as observed in Ti17 compared with Ti6242. Substantially consistent results were reported in the LFW Ti64 literature on the effect of an increase in the normal pressure thinning of the PAZ.<sup>[10]</sup> Increasing the amplitude or frequency was also reported to decrease the PAZ extent corroborating the results presented in this article.<sup>[9]</sup>

### C. Defects

The most detrimental and challenging feature in LFW Ti alloys is the removal/decomposition of the defects (oxides, intermetallics and voids) formed during welding and retained within the joint core. The presence of contaminants could jeopardize metal bonding and/or cause an embrittlement of the joint. The experiments performed in this study revealed the presence of scattered abnormal microstructural objects along the weld center line for the configurations using low PI and characterized by limited recrystallization and material blending. Both Ti17 and Ti6242 were subjected to the appearance of welding flaws in these conditions. The microstructural observations combined with local chemical and crystallographic analysis

showed that the configurations retaining defects were contaminated by copper residues. The latter is absent from the chemical composition of both alloys yet traces of copper could be significantly present on the row contact surfaces obtained by EDM as the ones welded in this study.<sup>[15]</sup>

The joints exhibiting flaws were characterized by the presence in the WL of fine voids within local microstructural formations resembling solidification microstructures. Furthermore, unlike in Ti17, these abnormal microstructures in Ti6242 revealed a quite singular dual-phase ( $\beta + \alpha$ ) micro-zone with traces of intermetallic  $\text{Ti}_2\text{Cu}$  formed within  $\alpha$  nodules. Investigations from the literature could lead one to impute these defects to a detrimental local copper enrichment as: (1) Copper dissolves easily in titanium and reduces the melting temperature, which might favor melting wear to occur; this could also result in the formation of  $\beta$  flecks creating microliquid pockets within the joint during LFW; (2) copper is an active  $\beta_{\text{Eutectoid}}$  element potentially causing the  $\beta \rightarrow \alpha + \text{Ti}_2\text{Cu}$  and/or  $\beta \rightarrow \beta_{\text{metastable}}$  transformations observed upon quenching from the  $\beta$  domain depending on the local amount of  $\beta_{\text{Stabilizer}}$  elements; (3)  $\beta$  fleck solidification could also be responsible for the formation of voids from shrinkage.

The configurations ensuring the highest PI combined with consistent grain fragmentation and material blending did not reveal the presence of any defects in the weld center line but homogeneous regular microstructures resembling those formed in  $\beta$  thermomechanical processing for both alloys. This encouraging result implies that the contaminants could be scattered within the whole WL with the help of material blending and enhanced diffusion by grain boundary motion. Indeed, it has been shown that the diffusion coefficients of Al atoms in migrating grain boundaries were remarkably larger than the corresponding coefficients reported for stationary boundaries.<sup>[16]</sup> Furthermore, commercially pure titanium grades were identified as remarkable oxygen getters that resorb the passive surface layer in ultra-high vacuum (UHV) at 450 °C justifying a probable complete disappearance of the oxides from the WL during LFW.<sup>[17]</sup> As a result, removing the altered surface layers from EDM would ensure the presence of solely passive layers with native oxides prior to welding and might improve the process robustness by limiting the risks of abnormal microstructure formation within the joint. Quite similar defects and abnormal microstructures were observed in LFW Ti-6.5Al-3.5Mo-1.5Zr-0.3Si and Ti6242 mono-material joints.<sup>[18,19]</sup> Those defects were characterized by a singular copper enrichment, which appeared highly detrimental to the mechanical durability, even after a PWHT at 950 °C.<sup>[18]</sup> Analogous evidence of local liquation phenomena was also reported in the literature on LFW Ni-based superalloys.<sup>[20,21]</sup>

#### D. Recrystallization and Texture

The microstructural changes in the Ti17 and Ti6242 joints induced by LFW revealed that the  $\beta$  thermomechanical processing occurring at the joint core resulted

in a massive grain fragmentation and in the development of a consistent  $\{110\}\langle 111 \rangle$  texture. The  $\alpha/\alpha'\{0001\}\langle 11\bar{2}0 \rangle$  texture formation upon cooling in Ti6242 is a direct consequence of such a  $\beta$  grain reorientation through the  $\beta \rightarrow \alpha/\alpha'$  transformation and variant selection from the BOR; such a texture could lead to an anisotropic behavior of the weld. The presence of recrystallized nuclei prone to grain growth upon heating might also play a role in further microstructural changes by influencing the homogenizing capability, defect dissolution and texture reduction/reorientation.

The results showed that the texture development is due to competing mechanisms between grain reorientation regarding the oscillating deformation conditions (increasing the texture intensity) and subgrain rotation through CDRX (reducing the texture intensity), both mechanisms being thermally activated and driven by the deformation conditions. Consequently, the  $\beta$  texture could be lowered by either (1) an enhanced recrystallization through an increase in strain and/or strain rate allowed by higher normal pressure, amplitude and frequency or (2) a limited longitudinal strain induced by a lower amplitude leading to lesser grain reorientations toward the oscillating direction. Such an impeded reorientation lowers the texture intensity despite exhibiting a drastically limited recrystallization. The microstructural characterization of the Ti6242 reference weld emphasized the fact that the  $\alpha\{0001\}\langle 11\bar{2}0 \rangle$  texture in the WL upon cooling results from the  $\beta\{110\}\langle 111 \rangle$  texture development during the process.<sup>[6]</sup> As a result the comparison between the welding configurations performed in this article were focused on the  $\beta/\beta_{\text{reconstructed}}$  texture. Indeed, the  $\alpha/\alpha'$  phase precipitation depends on complex  $\beta \rightarrow \alpha$  variant selection mechanisms, which are also influenced by the temperatures, cooling rates, residual stresses, crystal defects induced by plastic deformation, oscillating motion deceleration and several other complex mechanisms that could interfere with this transformation and the resulting texture development. Similar investigations on LFW of a near- $\beta$  alloy highlighted a comparable two-component  $\{110\}\langle 111 \rangle$   $\beta$  phase texture development and showed that a 40 pct decrease in frequency combined with a 1.5 times higher normal pressure resulted in an increased  $\beta$  texture and component heterogeneity.<sup>[22]</sup> A texture reduction of the  $\alpha'$  precipitates in LFW Ti64 joints was also reported when increasing the normal pressure.<sup>[10]</sup> However, information about the degree of grain fragmentation or material blending in LFW Ti alloys was not found in the literature.

The succinct experiment performed on grain growth upon heat treatment in the  $\beta$  domain for the  $A - 1$ ,  $A + 1$  and Ref Ti17 welds allowed major grain growth and the activation of recovery mechanisms resulting in: (1) a notable microstructure homogenization; (2) removal of traces of defects as well as the former distinct WL/TMAZ macro-zones; (3) reduction of the initial two-component  $\beta\{110\}\langle 111 \rangle$  texture intensity. Grain growth also led here to rotations of the initial

orientations of the nuclei resulting in the loss of the as-welded twin-symmetric texture. Moreover, the significant affinity of the copper to the  $\beta$  phase combined with an enhanced diffusion in migrating interfaces might have allowed the decomposition of the flaws into the bulk. This might have prevented grain boundary pinning by the defects in  $A - 1$  thus allowing a global grain growth in the former WL. Furthermore, the resulting highly similarly treated microstructures from Ref.  $A - 1$  and  $A + 1$  seemed to indicate that the degree of grain fragmentation did not have a significant impact on the final grain size. Consequently, the process parameters appeared to actually play a minor role in the microstructures after  $\beta$  annealing for the Ti17 welds.

## V. CONCLUSION

In this study the authors investigated the influences of the main linear friction welding process parameters (amplitude, frequency, normal pressure and axial shortening) on the microstructural changes and defect removal of two Ti alloy ( $\beta$ -metastable Ti17 and near- $\alpha$  Ti6242) mono-material butt joints. The following conclusions can be drawn:

1. The process duration can be lowered by an increase in the specific power input (PI) allowing enhanced material extrusion rates through an increase in the ratio between the normal pressure and local flow stress. This ratio is increased by a higher normal pressure and/or enhanced heat generation. The latter is driven by the plastic deformation in the weld and is mainly influenced by the oscillating motion configuration (amplitude and frequency).
2. Controlling the extents of the weld characteristic zones by the mean of process indicators such as the PI and/or process durations appeared challenging for the eight sets of process parameters tested here. Indeed, the extents of the joint and the PAZ were significantly higher when increasing the amplitude than when increasing the normal pressure while both exhibited similar burn-off rates and process durations. This behavior has been attributed to a larger heat generation in  $A + 1$  and an improved heat source removal in  $P + 1$ . The most efficient parameter for controlling the extents of the macro-zones appeared to be the normal pressure.
3. The presence of abnormal microstructures (*i.e.*, welding defects) and voids has been identified for the configurations exhibiting low material blending and limited  $\beta$  grain fragmentation in the WL during LFW. These defects were identified as resulting from a local copper enrichment initially present on the raw contact surfaces obtained by EDM. Such an enrichment might have resulted in microliquid  $\beta$  fleck pockets at the weld center line leading to the formation of voids and, in Ti6242, bimodal  $\alpha + \beta$  micro-zones with traces of  $Ti_2Cu$  precipitation. Diffusion enhanced by migrating boundaries combined with a favored material blending could have

helped in the defect resorption into the bulk for the “clean” configurations.

4. The two-component  $\beta$  phase  $\{110\}\langle 111 \rangle$  texture intensity could be lowered by increasing the degree of continuous dynamic recrystallization. The level of grain fragmentation was enhanced by increasing the plastic deformation and/or by using higher strain rates. This could be achieved by higher normal pressure, amplitude or frequency. However, low amplitude motion also decreased the texture intensity because of a lower grain alignment with the oscillation motion. The latter resulted in limited recrystallization favoring a smooth transition between the WL and TMAZ.
5. Grain growth of the recrystallized nuclei upon  $\beta$  annealing resulted in homogenized microstructures similar to those of the as-received prior  $\beta$  Ti17 for the reference and the two varied amplitudes. No grain boundary pinning or defects were observable after the heat treatment; a slight texture originating from the as-welded grain reorientation was still present.

## ACKNOWLEDGMENTS

The authors acknowledge the financial support from the French National Research Agency (ANR) through the OPTIMUM ANR-14-CE27-0017 project as well as the Spatial and Aeronautic Research Foundation, Hauts-de-France Region and European Regional Development Fund (ERDF) 2014/2020 for the funding of this work. The authors are also grateful to ACB for providing LFW welded samples and Airbus for their technical support.

## REFERENCES

1. Z. Liu and G. Welsch: *Metall. Trans. A*, 1988, vol. 19, pp. 527–42.
2. J.L. Huang, N. Warnken, J.-C. Gebelin, M. Strangwood, and R.C. Reed: *Acta Mater.*, 2012, vol. 60, pp. 3215–25.
3. M. Maalekian: *Sci. Technol. Weld. Join.*, 2007, vol. 12, pp. 738–59.
4. A. Vairis and M. Frost: *Wear*, 1998, vol. 217, pp. 117–31.
5. D. Ballat-Durand, S. Bouvier, M. Risbet, and W. Pantleon: *Mater. Charact.*, 2018, vol. 144, pp. 661–70.
6. D. Ballat-Durand, S. Bouvier, M. Risbet, and W. Pantleon: *Mater. Charact.*, 2019, vol. 151, pp. 38–52.
7. W. Li, A. Vairis, M. Preuss, and T. Ma: *Int. Mater. Rev.*, 2016, vol. 61, pp. 71–100.
8. A.R. McAndrew, P.A. Colegrove, C. Bühr, B.C.D. Flipo, and A. Vairis: *Prog. Mater. Sci.*, 2018, vol. 92, pp. 225–57.
9. P. Wanjara and M. Jahazi: *Metall. Mater. Trans. A*, 2005, vol. 36A, pp. 2149–64.
10. J. Romero, M.M. Attallah, M. Preuss, M. Karadge, and S.E. Bray: *Acta Mater.*, 2009, vol. 57, pp. 5582–92.
11. G. Lütjering and J.C. Williams: *Titanium*, Springer, Berlin, 2003.
12. G.W. Stachowiak and A.W. Batchelor: *Engineering Tribology*, Elsevier, Amsterdam, 2001.
13. J. Humphreys, G.S. Roher, and A. Rollett: *Recrystallization and Related Annealing Phenomena*, Elsevier, Amsterdam, 2017.
14. R. Turner, J.-C. Gebelin, R.M. Ward, and R.C. Reed: *Acta Mater.*, 2011, vol. 59, pp. 3792–803.
15. V.K. Manupati, G. Rajyalakshmi, M.L.R. Varela, J. Machado, and G.D. Putnik: *Innovation, Engineering and Entrepreneurship*, J.

- Machado, F. Soares, and G. Veiga, eds., Springer, Berlin, 2018, vol. 505, pp. 608–15.
16. K. Smidoda, W. Gottschalk, and H. Gleiter: *Acta Metall.*, 1978, vol. 26, pp. 1833–36.
  17. Y. Mizuno: *Temperature Dependence of Oxide Decomposition on Titanium Surfaces in UHV*. United States. <https://doi.org/10.2172/798917>.
  18. W. Li, J. Suo, T. Ma, Y. Feng, and K. Kim: *Mater. Sci. Eng. A*, 2014, vol. 599, pp. 38–45.
  19. J.M. Garcia and T.F. Morgeneyer: *Fatigue Fract. Eng. Mater. Struct.*, 2019, vol. 42, pp. 1100–17.
  20. K. Vishwakarma, O. Ojo, P. Wanjara, and M. Chaturvedi: *JOM*, 2014, vol. 66, pp. 2525–34.
  21. F. Masoumi, D. Shahriari, M. Jahazi, J. Cormier, and B.C.D. Flipo: *Metall. Mater. Trans. A*, 2017, vol. 48A, pp. 2886–99.
  22. E. Dalgaard, P. Wanjara, J. Gholipour, X. Cao, and J.J. Jonas: *Acta Mater.*, 2012, vol. 60, pp. 770–80.

**Publisher's Note** Springer Nature remains neutral with regard to jurisdictional claims in published maps and institutional affiliations.